Journal of Alloys and Compounds 778 (2019) 721–730

Contents lists available at ScienceDirect

Journal of Alloys and Compounds

journal homepage: http://www.elsevier.com/locate/jalcom

3D microstructure reconstruction of casting aluminum alloy based on serial block-face scanning electron microscopy

Jiawei Lu [a], Bo Chen [a, b, c, *], Xianping Liu [a, d], Fei Yang [a], Ian K. Robinson [a, b, e, **]

[a] School of Materials Science and Engineering, Tongji University, Shanghai 201804, China
[b] London Centre for Nanotechnology, University College London, London WC1H 0AH, UK
[c] Key Laboratory of Performance Evolution and Control for Engineering Structures of the Ministry of Education, Tongji University, Shanghai 200092, China
[d] Key Laboratory of Advanced Civil Engineering Materials (Tongji University), Ministry of Education, Shanghai 201804, China
[e] Division of Condensed Matter Physics and Materials Science, Brookhaven National Laboratory, Upton, NY 11973, USA

ARTICLE INFO

Article history:
Received 23 May 2018
Received in revised form
3 November 2018
Accepted 15 November 2018
Available online 19 November 2018

Keywords:
Aluminum alloy
Serial block-face scanning electron microscopy (SBFSEM)
3D microstructure reconstruction
Spatial morphology
Crack propagation

ABSTRACT

In this work, the inner microstructure of aluminum-silicon casting alloy was experimentally investigated to reveal the spatial morphology and phase distribution. Its industrial use is as a light-weight structural material. As a powerful three-dimensional (3D) imaging tool at the nano-scale, the serial block-face scanning electron microscopy (SBFSEM) was employed to investigate the specimens. After being 3D reconstructed, the images were visualized to identify preference for several specific intermetallics by quantitative analysis. It was found that these phases have certain relationships in spatial distribution and differences in spatial shapes. The spatial distribution of cracks was studied to understand their propagation and growth.

1. Introduction

Casting aluminum alloys play a critical role of substitution of conventional metal materials in the aerospace, automotive, shipbuilding and other machine manufacturing fields. Alloys are chosen for their excellent castability and high strength to weight ratio. Among the casting aluminum alloys, aluminum-silicon alloy is one of the most widely used.

It is well-known that almost all the performance characteristics of heterogeneous materials is attributed to their microstructural features. Because of the complex microstructure and large amounts of defects, different kinds of casting aluminum alloys vary significantly in certain mechanical properties.

Many previous investigations have addressed the relationship between microstructure and mechanical performance of aluminum-silicon alloy. Xiangqun Ding found the mobility of defects and stress concentration are closely related in the Al-Mg-Si alloys inner microstructure [1]. Mohamed Iben Houria thought secondary dendritic arm spacing has a significant influence on the fatigue age of certain aluminum alloys under the torsional loading condition [2]. Chen found with increasing the size and number of Si particles, interface peeling between particles and matrix appears frequently, which reduces the resistance to fatigue cracks [3]. The spatial distribution of coarse-grained particles, as well as their size and volume fraction in the Al matrix, affects the strength of the composite [4]. Ganesh and Chawla experimentally investigated the influence of Si particle orientation on the fatigue and tensile properties [5] and Campbell found fatigue cracks always originates from pores and shrinkage defects [6]. Payne found that the microstructure of coarse second phase particles with large area significantly affects the crack initiation [7].

Most of the structure research, such as those reported above, were based on the two dimensional sections obtained by conventional methods, such as the metallographic microscope or scanning electron microscope (SEM). For the quantitative characterization of size, shape, connectivity and spatial distribution of pores, grains and intermetallic compounds, it would be very helpful if the data in

* Corresponding author. School of Materials Science and Engineering, Tongji University, Shanghai 201804, China.
** Corresponding author. London Centre for Nanotechnology, University College London, London WC1H 0AH, UK.
E-mail addresses: bo.chen@tongji.edu.cn (B. Chen), i.robinson@ucl.ac.uk (I.K. Robinson).

https://doi.org/10.1016/j.jallcom.2018.11.188
0925-8388/

vertical direction (z axis) was statistically significant too. Some researchers made quantitative assessment of 3D microstructures from a few 2D image sections with a statistical synthetic model [8], but it didn't really return 3D information. So it is inaccurate and unrepresentative to estimate the spatial microstructure information by stereological methods.

A method that can reveal a material in its entirety is quite necessary. So the three-dimensional microstructure imaging technique (3D-MIT) has been applied to aluminum alloy researching field. Typically, 3D-MIT is divided into two kinds of classifications according to whether the sample is destroyed or not during the measurements. One is nondestructive, such as X-ray computed tomography based on the X-ray absorption and scattering including laboratory and synchrotron X-ray based micro- and nano-tomography [9–11]. The other one called serial sectioning tomography that is destructive, which uses different mechanical methods to obtain serial section images. Focused ion beam (FIB), metallographic serial polishing (MSP), serial block-face (SBF) are 3 of these types of imaging modalities. FIB is expensive, observable area is too small for region of interest and it may result in sample damage during direct milling by high-energy ions [12,13]. MSP is low cost but its mechanical damage is too much and resolution (in z axis) is not enough for nano- or micro-scale investigation [14,15]. Considering the balance between area of observed region and influence of mechanical damage during measurements, in our work, the 3D detailed features of Al-Si casting alloy was imaged by serial block-face scanning electron microscope (SBFSEM), which uses an SEM with a built-in serial sectioning ultramicrotome for collect high-quality, high-resolution serial images [16,17]. Chen et al. have investigated 3D structure of a barrier marine coating [18]. Hashimoto et al. have highlighted the strategies for minimizing artifacts caused by SBF system and acquired many 3D images for a variety of metallic and coated systems [19,20]. Being able to do the 3D microstructure visualization, reconstruction from continuous 2D information is a key process where many algorithms were applied, such as filtering, binarization and thresholding. A particular effort of this study is on the quantitative analysis of critical structural parameters of Al-Si casting alloy, which could enable the optimization of manufacturing process and the numerical investigation for the improvement of mechanical performance in the future.

2. Experimental

The chemical composition of the Al-Si casting alloy investigated in this study is given in Table 1. Samples with the same casting process and heat treatment, “T6 conditions”, were used in this experiment.

A series of uniaxial strain-controlled fatigue tests were conducted on the samples at the strain amplitude of 0.3 and frequency of 1 Hz. The samples were then observed at voltage of 15 kV by a Zeiss Sigma 300VP SEM equipped with an energy-dispersive spectrometer (EDS). Zeiss Sigma 300VP SEM equipped with Gatan 3view chamber as shown in Fig. 1, one indoor ultramicrotomy system was used to section samples and to image serially prior to reconstructing 3D images.

Sample preparation is a challenge for SBFSEM measurements. The Al-Si aluminum alloy samples were firstly wire cut to strip-shaped pieces with size of 1*1*10 mm. For ruling out the cutting damage and getting an appropriate shape, conventional ultramicrotomy (Leica EM UC7) with a glass knife was used to reshape a strip piece into a cascade quadrangle, as shown in Fig. 1, whose minimum section area is approximately 300*300μm. Then adhere the sample to a one-off sample stage with super glue and conductive silver glue. Ultramicrotomy can cause artificial defects due to pulling off the hard phase or compression of the soft phases [21]. So, before recording the images by SBFSEM, we removed the residual damage generated during the sample preparation by approach operation. In order to minimize the artifact and achieve the better resolution in z axis [22], 0.2 mm/s cutting speed and 30 nm slice thickness were set up to the 3D record process. The 3D measurements were done at an acceleration voltage of 2 kV. Finally, choose a representative region of the microstructure with appropriate brightness, contrast and magnification. Selection of this region of interest is vital as it is desirable to capture complete research objects encompassed in the selected volume, which can be reconstructed into 3D images and can be quantitatively analyzed.

3. Discussion and result

3.1. Intermetallics and other compounds

Because of the incident and inevitable systematic error during the imaging process, series of pre-processings including alignment, contrast matching, filtering are carried out to the original images for segmentation which is to separate the region of interest from the matrix through specific gray-scale thresholding. Thus, it's essential to truly identify each phase with different gray values in the obtained images. The various intermetallic phases were identified in this report by considering the BSE grayscale value/average atomic number curve, distribution characteristic and feature morphologies. To reconstruct the separated regions, volume rendering and surface generating was used to stack slices and to visualize the 3D structure. To quantitatively analyze the microstructure, each individual object was labeled and sequences of measured data of labeled objects could be measured by specific algorithm.

On the one hand, EDS can't be employed when the SBFSEM is working; on the other hand, the observed phases can't be found and tested by EDS after the BSE images recording due to the destructive experiment process. Under the premise of knowing the existing phases in this alloy, one method was used to identify which intermetallics the different phases in the BSE images are by the relationship among average atomic number, BSE coefficient and grayscale values [19]. In this study, several known intermetallics and silicon compounds in this typical casting Al-Si alloy [20], Mg_2Si, Al_2Cu, $Al_5Mg_8Si_6Cu_2$, $Al_{15}(Mn,Fe)_3Si_2$, Al_5FeSi and $Al_8Mg_3FeSi_6$, were inputted to a short self-coded python program. As the result, it calculates values of average atomic number, BSE coefficient and corresponding gray scale, and plot the graph which was used to deduce the intermetallics in this paper, as shown in Fig. 2. However, sometimes the grayscale value of one phase, which is measured from BSE image set, is in a certain range, rather than an exact value because of the systematic error. In this range, we may find more than one intermetallics (see Fig. 2). In this case, an intermetallic can be identified by combining consideration of the reconstructed 3D morphology because of its certain specific spatial structures.

Table 1
Chemical composition of investigated casting alloy (wt. %).

Elements	Si	Fe	Cu	Mn	Mg	Ni	Zn	Sn	Others	Al
%	6.2	1.2	3.0–4.0	<0.50	<0.10	<0.35	<1.0	<0.25	<0.50	Balance

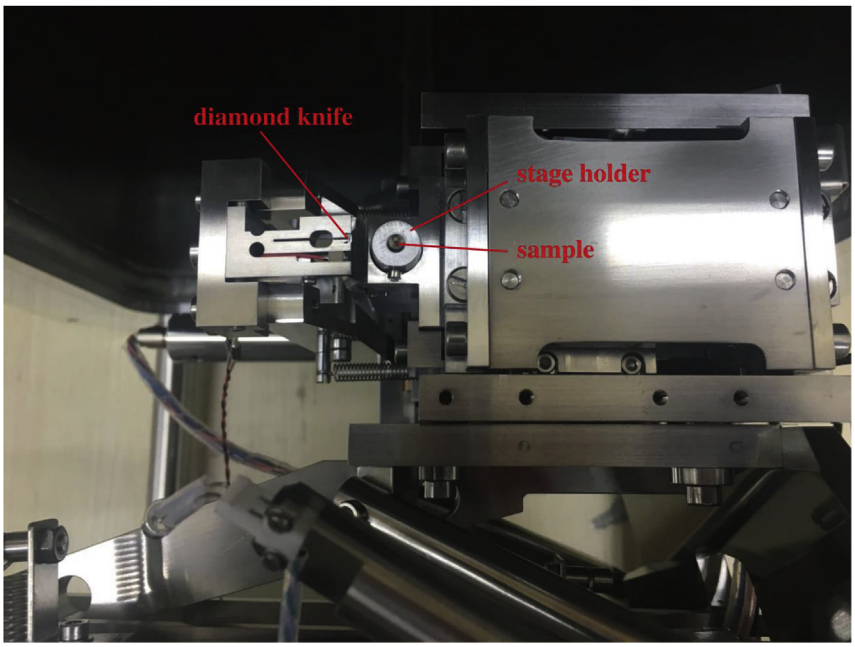

Fig. 1. The inside construction of SBFSEM chamber.

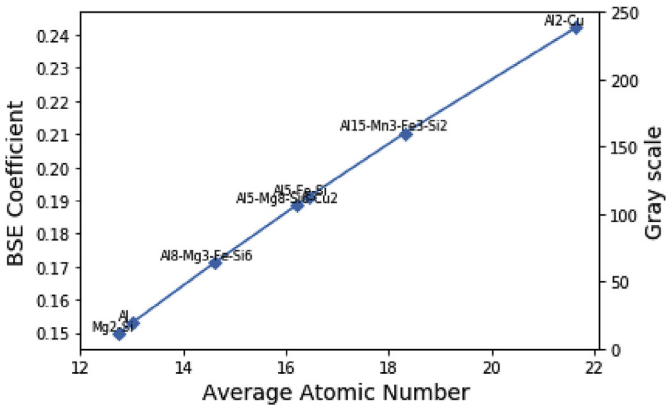

Fig. 2. Line chart of grayscale level, where variation of BSE coefficient with average atomic number and grayscale of intermetallics are contained.

3.1.1. Al_2Cu

By observing the SE micrograph and EDS images, it is easy to determine that the α-Al matrix is separated by the interdendritic network which consists of a large amount of eutectic Si particles and intermetallics, as presented in Fig. 3. It shows the overall structure of this sample and the distribution of 4 main elements (Al, Si, Cu and Mg) within it.

In Al-Si alloy, one common intermetallic, Al_2Cu, is easy to identified and segmented due to its high contrast relative to other phases within the range between 200 and 250 in grayscale value. Being distinguished by spatial shape, Al_2Cu can be classified into two categories: blocky-shaped structure (pro-eutectic) and mesh-shaped structure (eutectic). Here, two kinds of Al_2Cu in the sample have been reconstructed to observe their obviously different spatial shapes from overlook images as shown in Fig. 4. Restricted by the integrity of the original data, only the blocky-shaped Al_2Cu was completely reconstructed in Z direction relatively.

In particular, it was found that the eutectic Al_2Cu prefers to fracture into smaller particles along the limited length in z direction, rather than preserve spatial integrity like pro-eutectic Al_2Cu. Each independent block in 2D slices were labeled in different colors by using Avizo 'Labeling' module and enabling the 'XY planes' interpretation. The more colors one slice containing means the more separated phases tend to be, and they are presented in Fig. 5 with the slice number increasing.

For each slice, the total area of all the independent phases which are marked in different colors and the counts of independent phases were figured out to plot two graphs, as shown in Fig. 6, for validating the speculation above. Under the almost same y-scale, the tendency of independent phase number shows the remarkable difference between the two kinds of Al_2Cu. With the decrease of total area of each slice, the independent phase number of mesh-shaped Al_2Cu increases noticeably, while the blocky Al_2Cu always keep stable. From the 3D perspective, the boundary (where total slice area is small) of mesh-shaped Al_2Cu has more branches (independent phases on slices), which means this kind of grain is much coarser than blocky Al_2Cu.

3.1.2. $Al_5Mg_8Si_6Cu_2$

This alloy commonly has as a dominant impurity copper, which forms complex intermetallics during solidification. Solid solution and aging treatments increase the solubility of the eutectic Al_2Cu. Consequently, the relative volume fraction of blocky phase (pro-eutectic Al_2Cu) increase to some degree, which results in some small size phases that was masked by mesh-shaped Al_2Cu is readily disclosed much more apparently [20]. One MgCu-based intermetallic which was reported in acicular or elliptical shape(2D) is $Al_5Mg_8Si_6Cu_2$ which is usually found next to the Al_2Cu phase (both pro-eutectic and eutectic) [23,24]. From the BSE images set, we found one phase whose grayscale value was measured in the approximate range between 100 and 140 where there are two known compounds, Al_5FeSi and $Al_5Mg_8Si_6Cu_2$ between this range in Fig. 2. Additionally, according to the morphology of this phase, this intermetallic which was found around the blocky Al_2Cu, as shown in Fig. 7 is considered to be $Al_5Mg_8Si_6Cu_2$. However, from the view of spatial variation, the $Al_5Mg_8Si_6Cu_2$ phase in ellipse actually is not ellipsoid, but similar to elliptic cylinder always

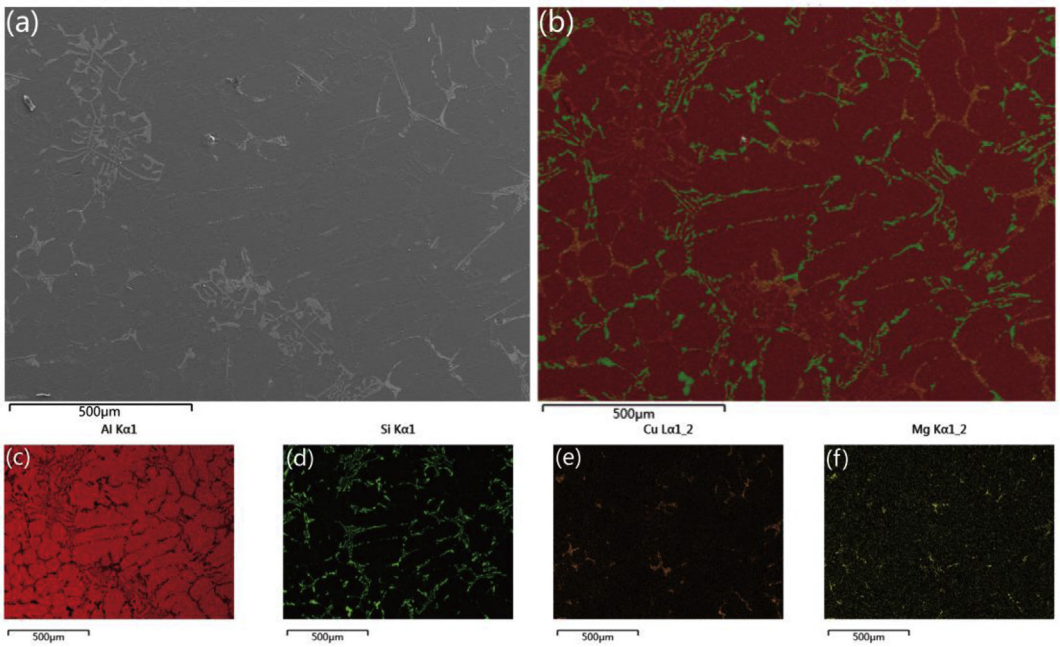

Fig. 3. The SEM image and EDS elemental mappings of the overall structure of the sample. (a) Second electron (SE) micrograph of the sample, (b) EDS mapping of the same region of the sample as shown in panel a, (c)-(f) Al, Si, Cu and Mg element distribution, extracted from panel b, in the same region as shown in panel a.

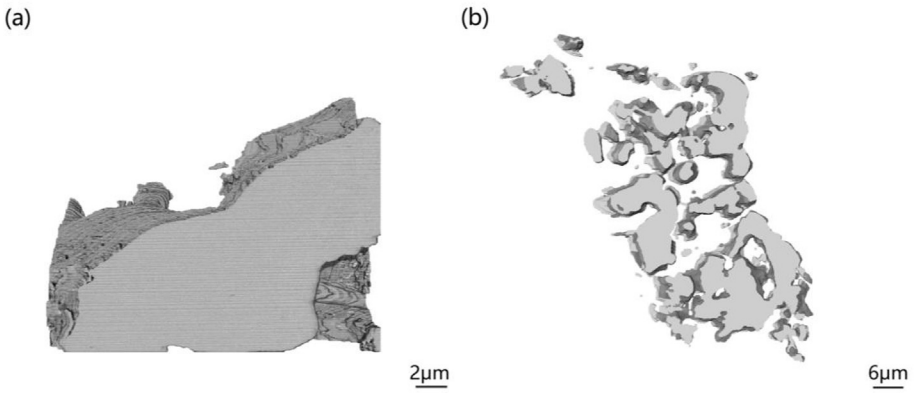

Fig. 4. Reconstruction image of two kinds of Al_2Cu, pro-eutectic is (a), the eutectic is (b).

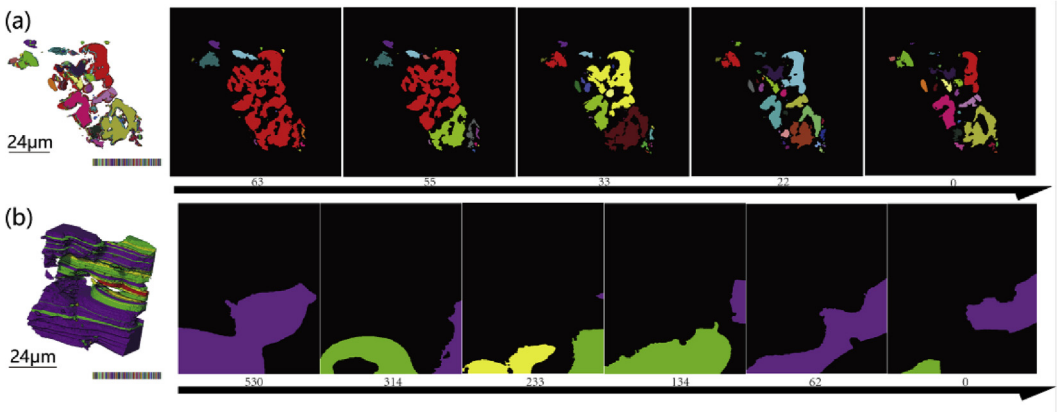

Fig. 5. The reconstruction images of labeling slices of two kinds of Al_2Cu by enabling the 'XY planes' interpretation (a) is the labeling 3D reconstructive image of eutectic Al_2Cu and the respective slices No. 63, 55, 33, 22, 0. (b) is the labeling 3D reconstructive image of pro-eutectic Al_2Cu and the respective slices No. 530, 314, 233, 134, 62, 0.

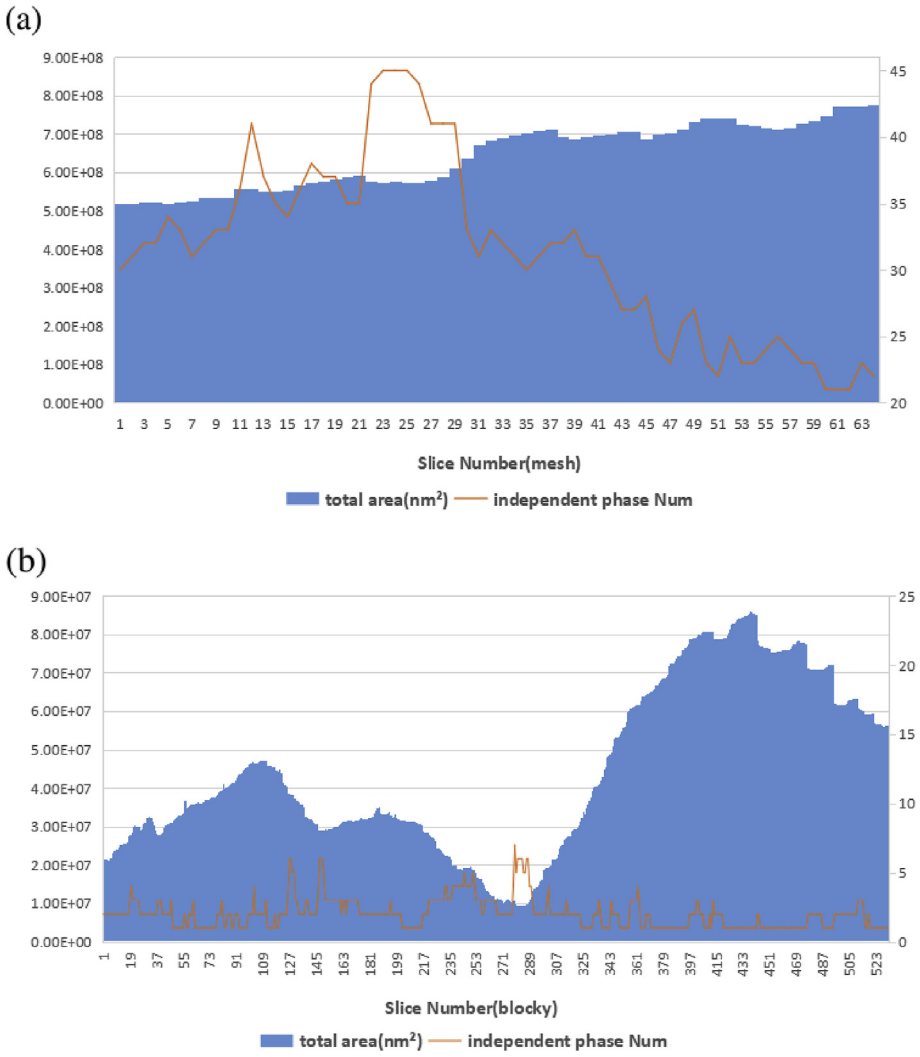

Fig. 6. The correlative trends between total area and independent phase number in each slice, (a) is eutectic Al_2Cu and (b) is pro-eutectic Al_2Cu.

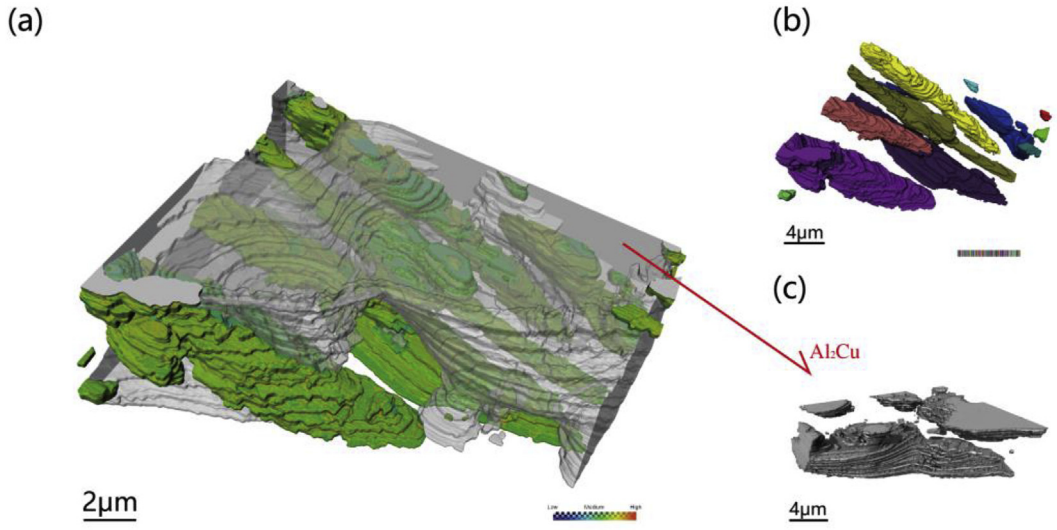

Fig. 7. The reconstruction images of $Al_5Mg_8Si_6Cu_2$ which is in acicular shape (a) perspective 3D structure of $Al_5Mg_8Si_6Cu_2$ in acicular shape around pro-eutectic Al_2Cu; (b) each independent $Al_5Mg_8Si_6Cu_2$ particle is marked in different labeling color; (c) Al_2Cu envelope. (For interpretation of the references to color in this figure legend, the reader is referred to the Web version of this article.)

carrying a long tail, as shown in Fig. 8a. The description of shape in the past (ellipse) may has been misguided due to observing the info-limited 2D section structure, just as shown in the top-view of Fig. 8b (section of overlook).

As for the surrounding of mesh-shaped eutectic Al_2Cu in Fig. 9 (which was not completely reconstructed because of the limited data), 'acicular shapes' always appear at the gap between close phases. 'Elliptical shape' is always found to exist in the relatively spacious gap. But in the z direction, these ellipses possibly turn to stripes following a long tail. The spatial morphology of $Al_5Mg_8Si_6Cu_2$ seems to fill the gaps between matrix or other phases, which may suggest the crystallization time of this phase is relatively late.

From our view, these two shapes (ellipse or acicular) can be unified to one category, striped-shape, for the large aspect ratio. This is a good example which demonstrates that compared with 2D structure, the 3D structure is more accurate to identify phases. It is similar with what Seifeddine had suggested, the formation of different shapes of $Al_5Mg_8Si_6Cu_2$ probably associated with Al_2Cu phase during final solidification [25,26].

For the obvious acicular shape structures shown in Fig. 7a and b, quantitative calculations have been done to analyze the spatial morphology. Using labeling module of Avizo by enabling the '3D' interpretation outputs Fig. 7b where each spatially individual particle was highlighted in different colors. Spatial geometric statistic of 13 particles have been accurately calculated by using 'label analysis' module based on the reconstructed 3D structure, as shown in Table 2. It is manifest that the length-wide ratio (Feret's diameters was introduced in this statistics) of the particle is positively correlated with its volume, which is referred by Fig. 10. The correlation coefficient of these two variables is calculated to be 0.565. It is likely that those particles with low length-width ratio and small volume were not reconstructed completely. Filtering out particles whose volume is smaller than 1×10^9 nm^3 (1 μm^3), we found the length-width ratio of remainders (sum of the Length3d/sum of the Width3d) is 5.32.

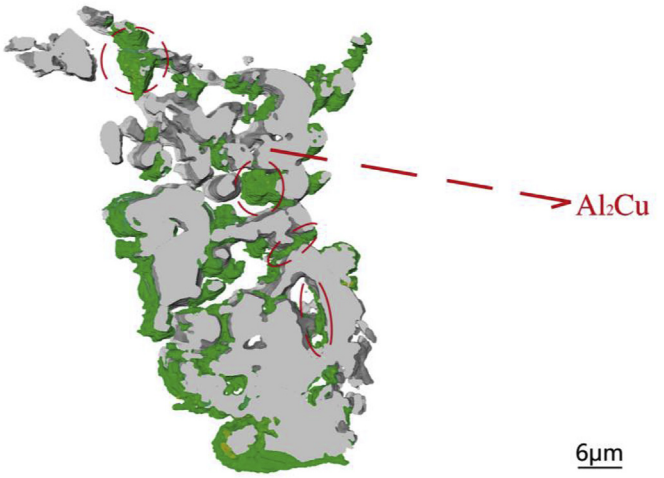

Fig. 9. Incomplete 3D structure of $Al_5Mg_8Si_6Cu_2$, which is in green and around mesh-shaped eutectic Al_2Cu. Some seem like 'acicular shape', the others seem like 'elliptical shape', which were both highlighted in Dotted line frame. (For interpretation of the references to color in this figure legend, the reader is referred to the Web version of this article.)

3.1.3. $Al_{15}(Mn,Fe)_3Si_2$

Around AlMgSiCu phase, an Fe-containing intermetallic was found [27]. This compound as shown in Fig. 11a, $Al_{15}(Mn,Fe)_3Si_2$, was identified by combining the spatial shape of small platelet and the graph shown in Fig. 2. The average atomic number and BSE coefficient were calculated to be 18.31 and 0.21. The grayscale range measured in the BSE images, such as Fig. 11b, is between 140 and 180 which is consistent with the curve in Fig. 2.

3.2. Cracks and defects

The poor alloy ductility is attributed to the coarse intermetallics,

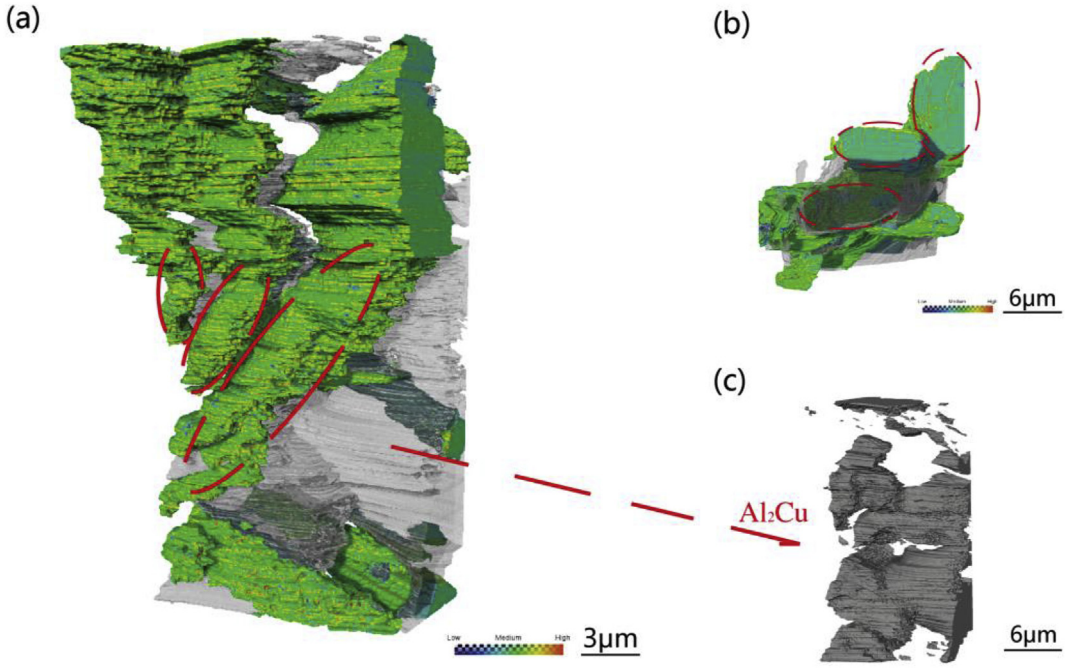

Fig. 8. The reconstruction images of $Al_5Mg_8Si_6Cu_2$ which carries a long tail (a) perspective 3D structure of $Al_5Mg_8Si_6Cu_2$ in cylinder shape with long tails; (b) the misleading section characterization like ellipse; (c) Al_2Cu envelope.

Table 2
Geometric information of individual particles.

index	Length3d (nm)	Width3d (nm)	Area3d (nm^2)	Volume3d ($\times 10^9$ nm^3)	Log (Volume3d)	length-width ratio
1	15784.6	4635.87	226734000	68.32	10.83	3.40
2	1756.14	710.813	4169540	0.46	8.66	2.47
3	18248.6	2903.27	151580000	49.34	10.69	6.29
4	1341.14	762.426	2594270	0.26	8.42	1.76
5	1906.65	741.697	3447300	0.37	8.57	2.57
6	2278.71	698.7	4847920	0.47	8.67	3.26
7	20839.4	3197.43	184738000	41.84	10.62	6.52
8	9107.38	3186.78	78491600	23.44	10.37	2.86
9	11850.2	2166.09	84569700	22.17	10.35	5.47
10	1710.29	981.361	4853540	0.71	8.85	1.74
11	20653.8	2903.95	169037000	43.58	10.64	7.11
12	5833.72	1080.36	14027500	2.12	9.33	5.40
13	11865.7	1403.66	28030400	2.75	9.44	8.45

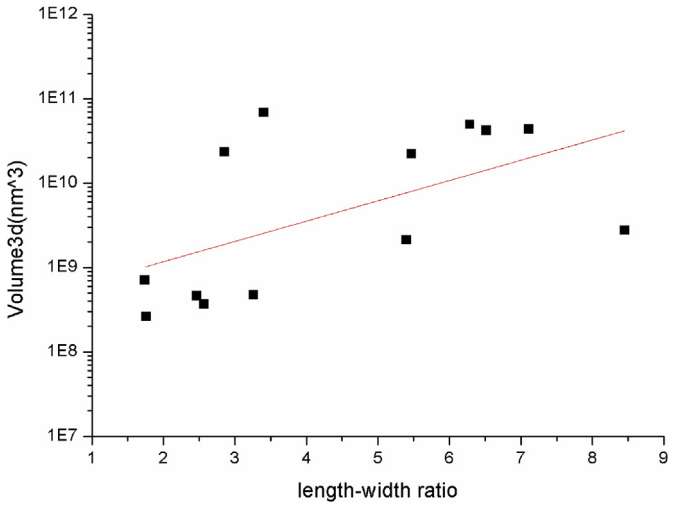

Fig. 10. The scattering plot of the particles recorded in Table 2 regarding the volume and length-wide ratio.

which leads to unsteady crack propagation through a sequence of fracturing events in connecting phases [28]. The dataset, as shown in Fig. 12, suggests that the trends of cracks in Al matrix is towards the brittle intermetallics such as Al_2Cu.

When cracks propagate to the intermetallics, 3 factors are introduced which affect the crack propagation: intermetallic brittleness, defects along grains boundary, intermetallic morphology. When the cracks spread to intermetallics, 3 common growing types may happen to the cracks, as shown in Fig. 13.

For some intermetallics in plate shape, such as Al_2Cu or $Al_5Mg_8Si_6Cu_2$, crack type 1 happens much more frequently. This is probably because the high brittleness of these phases plays the most important role in the crack propagation. In this growing type, the crack is always found merely inside the intermetallic, which concluded that the brittle intermetallics act as the crack initiator in general, which is exhibited in Fig. 14 and Fig. 15a and b. As to type 2, if the defects gathers along the grains boundary, where defects indeed exist [29], the cracks tend to grow following the boundary because of the stress concentration. Another propagation type 3 illustrates an inductive effect for the zigzag morphology and irregular distribution in small space. As shown in Fig. 12, the cracks were found near the eutectic Al_2Cu. Cracks tend to spread following small paths inside the intermetallics, as marked in red in Fig. 15c. To a certain extent, these kinds of cracks are theoretically restrained by the spatial morphology because the longer propagation distance and more energy are required for crack propagation.

We found in some regions, the cracks tend to concentrate around the brittle phase, the cracks existing in the Al matrix and brittle intermetallics are separated into two colors by the Avizo

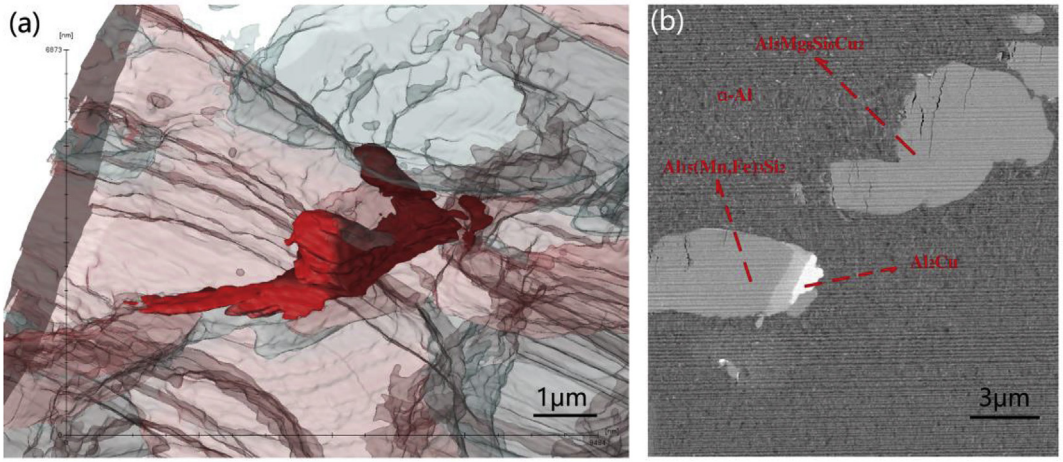

Fig. 11. The reconstruction images of $Al_{15}(Mn,Fe)_3Si_2$ which is in the shape of small platelet, (a)3D reconstruction of $Al_{15}(Mn,Fe)_3Si_2$ in red which was surrounded by Al_2Cu (in transparent grey) and $Al_5Mg_8Si_6Cu_2$ (in transparent red), (b) one original BSE image of the slice stack. (For interpretation of the references to color in this figure legend, the reader is referred to the Web version of this article.)

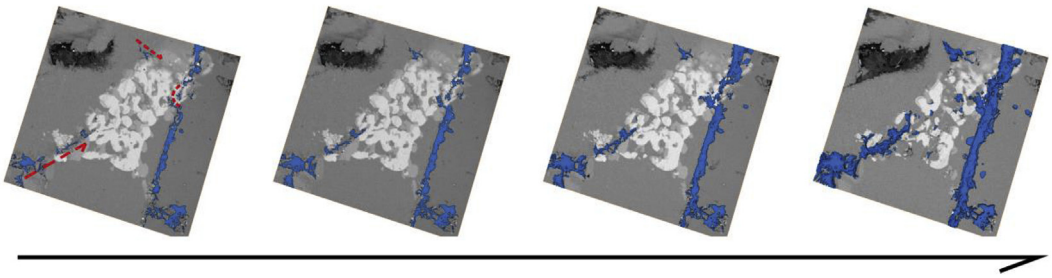

Fig. 12. The propagation of cracks around the brittle Al_2Cu and $Al_5Mg_8Si_6Cu_2$ in several representative slices, whose trend is marked in red line. Cracks are highlighted in blue, the background is the BSE images. (For interpretation of the references to color in this figure legend, the reader is referred to the Web version of this article.)

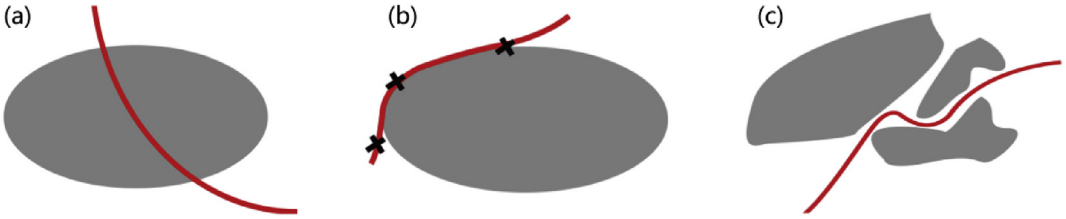

Fig. 13. Three types of crack propagation. The red line represents cracks. Gray objects represent intermetallics with different morphology. (a) represents type 1. (b) represents type 2. Black crosses in (b) represent the defects along the boundary. (c) represents type 3. (For interpretation of the references to color in this figure legend, the reader is referred to the Web version of this article.)

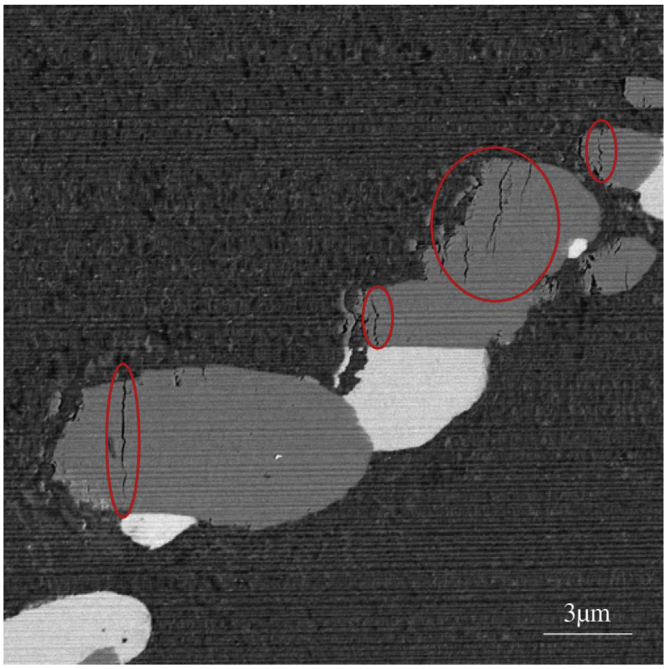

Fig. 14. One original BSE image of the slice stack showing the cracks of type 1.

image logic algorithm, as shown in Fig. 16a. It is apparent that the cracks in the brittle phase, which are in purple are much more than in blue which are the cracks in Al matrix. Particularly, when numerous cracks appear in one certain brittle phase, it will be normal to find corresponding cracks appearing in the adjacent matrix, which was highlighted in Fig. 16b. In the other words, it is very rare that the isolated cracks appear in the aluminum matrix.

A chamfer distance map, an algorithm where each voxel in the region of interest will be assigned a value depending on the distance to the nearest object boundary, was introduced to demonstrate the phenomenon above. The boundary voxels of the object are assigned a value of zero whereas the assigned value increases as the distance increases. Applying the distance map algorithm to the binary image of the Al matrix gives a gray level image where each voxel intensity represents the minimal distance in voxels from the matrix envelope which is the boundary between Al matrix and brittle phase, as shown in Fig. 17a. Then masking the cracks in the Al-matrix to the distance map gives the distance from each voxel in matrix to the closest voxel in boundary. The counts of voxels in each group which was classified by the distances was plotted in the Fig. 17b which shows the number of crack voxels located at a given distance from the matrix envelope. The distance values in voxels are obviously concentrated in the range within 235 nm and all the voxels are within 1800 nm from the boundary. Consequently, the cracks in the matrix are always close to the brittle phases where cracks have existed. This phenomenon can be explained as follows: once a given intermetallic fractured, the stress relaxation will happen to the surrounding Al matrix, leading to a transfer of load to adjacent matrix [29].

4. Conclusion

The 3D spatial structure of the aluminum-silicon casting alloy sample was revealed by serial block-face scanning electron microscopy (SBFSEM). SBFSEM is a promising characterizing method to be a useful tool to investigate the spatial microstructures of soft alloys. Several specific intermetallics were identified here by their reported morphology and the relationship between average atomic number, BSE coefficient and grayscale values. The spatial shape and distribution of these phases were visualized by 3D reconstruction using Avizo software. Pro-eutectic Al_2Cu is found to have a blocky shape, while the eutectic Al_2Cu tends to be relatively coarser with a mesh-shape. $Al_5Mg_8Si_6Cu_2$ was identified as striped shape only by inferring its spatial morphology in three dimensions, rather than the acicular and elliptical shapes as reported in the previous literature based on 2D information. Grayscale values, BSE coefficient and average atomic number were used to identify $Al_{15}(Mn,Fe)_3Si_2$.

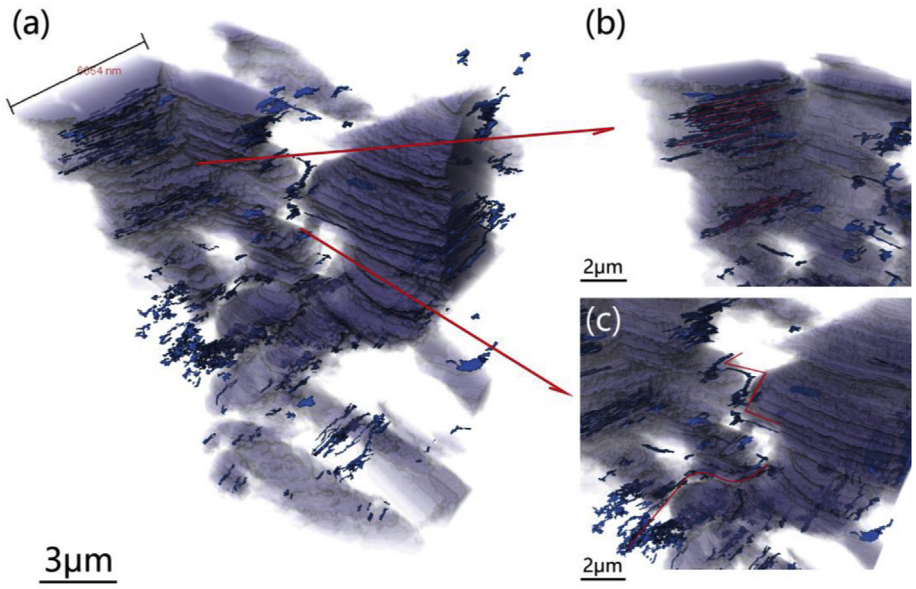

Fig. 15. The cracks which are marked in blue and their distribution in Al matrix (colorless region) and brittleness phase (transparent region which was rendered by Avizo) were visualized in (a). (b) The reconstruction image of crack 'type 1', (c) The reconstruction image of crack 'type 3'. (For interpretation of the references to color in this figure legend, the reader is referred to the Web version of this article.)

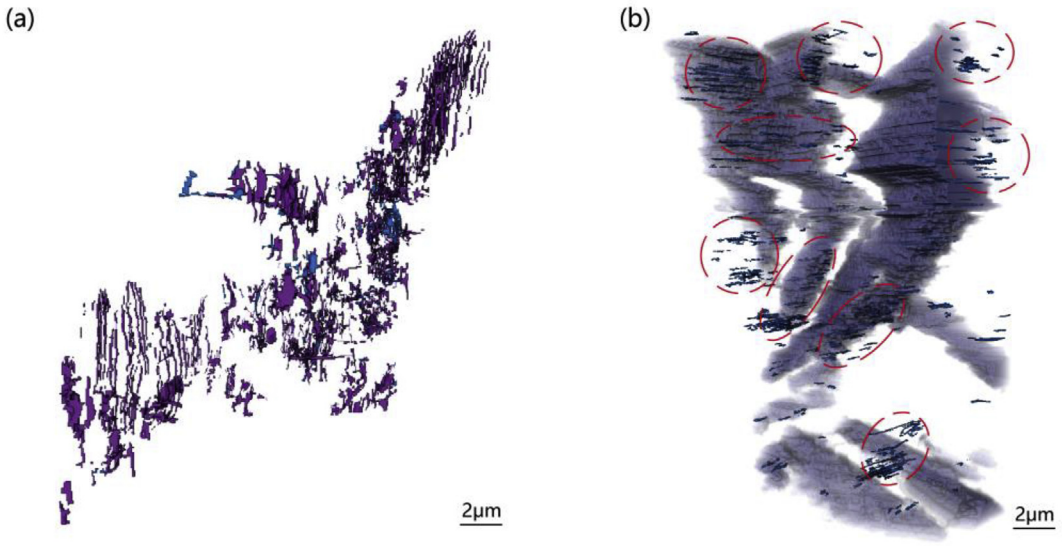

Fig. 16. The relationship of the distribution of cracks (a) the separated cracks in two colors: the purple is in brittle phases and the blue is in the Al matrix. (b) when the cracks appear in the brittle phase (transparent region), the corresponding cracks always appear in the surrounding matrix (colorless region). (For interpretation of the references to color in this figure legend, the reader is referred to the Web version of this article.)

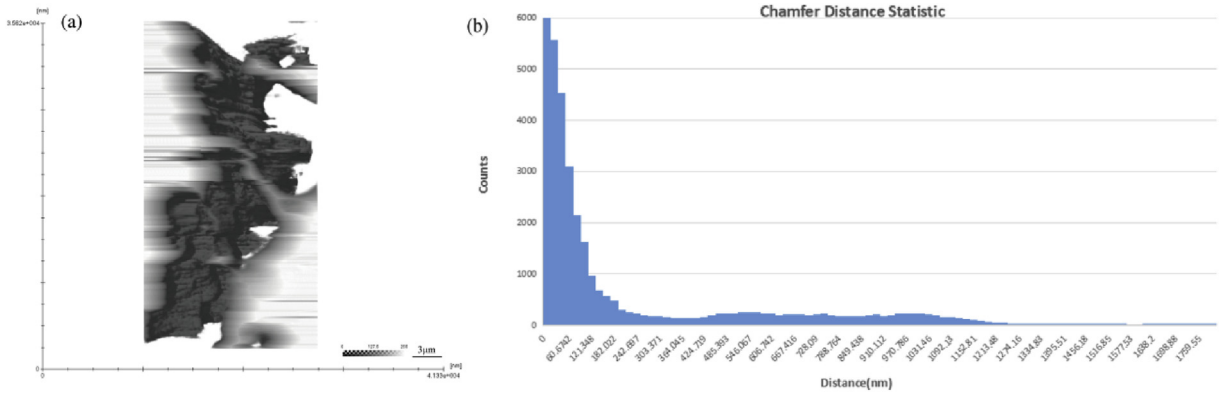

Fig. 17. The chamfer distance map and the histogram which was plotted by distance map data (a) the distance map illustrates that the greater the gray intensity is, the closer the objects to the boundary (b) Histogram showing the counts of voxels corresponding to the different distances.

Based on the spatial distribution data, the propagation and growth mechanism of cracks in this alloy was thought to be concentrated because of the brittle phases and stress transfer. Further quantitative analysis and simulations of the 3D structure could be performed with better original data in the future.

Acknowledgements

This work was supported by the TongJi University, China, through the High-level Talent Programme “Materials Nano-structure” with grant Numbers 152221 and 152243, and the “Shanghai PuJiang Talent Program” under grant number 18PJ1410400. Work at Brookhaven National Laboratory was supported by the U.S. Department of Energy, Office of Science, Office of Basic Energy Sciences, under Contract No. DE-SC00112704. The SBFSEM measurements were carried out at the School of Materials Science and Engineering, Tongji University, China.

References

[1] X.Q. Ding, G.Q. He, C.S. Chen, Study on the dislocation sub-structures of Al–Mg–Si alloys fatigued under non-proportional loadings, J. Mater. Sci. 45 (15) (2010) 4046–4053.
[2] M.I. Houria, Y. Nadot, R. Fathallah, et al., Influence of casting defect and SDAS on the multiaxial fatigue behaviour of A356-T6 alloy including mean stress effect, Int. J. Fatig. 80 (2015) 90–102.
[3] Z.Z. Chen, K. Tokaji, Effects of particle size on fatigue crack initiation and small crack growth in SiC particulate-reinforced aluminium alloy composites, Mater. Lett. 58 (17–18) (2004) 2314–2321.
[4] J.G. Kim, J.I. Bang, Y.J. Kim, Y.H. Park, Effect of SiC particle size and particle distribution on microstructure and mechanical properties of A359/SiC~p using powder metallurgy, Kor. J. Met. Mater. 51 (2013) 857–864.
[5] N. Chawla, R.S. Sidhu, V.V. Ganesh, Three-dimensional visualization and microstructure-based modeling of deformation in particle-reinforced composites, Acta Mater. 54 (6) (2006) 1541–1548.
[6] K. Gall, N. Yang, M. Horstemeyer, et al., The debonding and fracture of Si particles during the fatigue of a cast Al-Si alloy, Metall. Mater. Trans. A 30 (12) (1999) 3079–3088.
[7] J. Payne, G. Welsh Jr., R J C, et al., Observations of fatigue crack initiation in 7075-T651, Int. J. Fatig. 32 (2) (2010) 247–255.
[8] H.K. Park, J. Jung, H.S. Kim, Three-dimensional microstructure modeling of particulate composites using statistical synthetic structure and its thermo-mechanical finite element analysis, Comput. Mater. Sci. 126 (2017) 265–271.
[9] D.J.D. Rosier, A. Klug, Reconstruction of three dimensional structures from electron micrographs, Nature 217 (5124) (1968) 130–134.
[10] G. Li, R. Shi, Q. Fan, et al., Reconstruction and quantitative characterization of the three dimensional microstructure model of TC6 titanium alloy based on dual-energy X-ray microtomography, Mater. Sci. Eng., A 675 (2016) 212–220.
[11] S.S. Singh, C. Schwartzstein, J.J. Williams, 3D microstructural characterization and mechanical properties of constituent particles in Al 7075 alloys using X-ray synchrotron tomography and nanoindentation, J. Alloys Compd. 602 (2) (2014) 163–174.
[12] Y. Lu, Y.L. Chiu, I.P. Jones, Three-dimensional analysis of the microstructure and bio-corrosion of Mg–Zn and Mg–Zn–Ca alloys, Mater. Char. 112 (2016) 113–121.
[13] C.R. Mayer, J. Molina-Aladareguia, N. Chawla, Three dimensional (3D) microstructure-based finite element modeling of Al-SiC nanolaminates using focused ion beam (FIB) tomography, Mater. Char. 120 (2016) 369–376.
[14] M. Li, S. Ghosh, T.N. Rouns, et al., Serial sectioning method in the construction of 3-D microstructures for particle-reinforced MMCs, Mater. Char. 41 (1998) 81–95.
[15] J.M. Jung, H.Y. Ji, H.J. Jeong, et al., Three-dimensional characterization of SiC particle-reinforced Al composites using serial sectioning tomography and thermo-mechanical finite element simulation, Metall. Mater. Trans. A 45 (12) (2014) 5679–5690.
[16] W. Denk, H. Horstmann, Serial block-face scanning electron microscopy to reconstruct three-dimensional tissue nanostructure, PLoS Biol. 2 (11) (2004) e329.
[17] Gatan Inc., the Product Introduction of 3View System, 2018. http://www.gatan.com/products/sem-imaging-spectroscopy/3view-system/. (Accessed 3 April 2018).
[18] B. Chen, M. Guizar-Sicairos, G. Xiong, et al., Three-dimensional structure analysis and percolation properties of a barrier marine coating, Sci. Rep. 3 (2013) 1177.
[19] T. Hashimoto, G.E. Thompson, M. Curioni, et al., Three dimensional imaging of light metals using serial block face scanning electron microscopy (SBFSEM), Mater. Sci. Forum 765 (2013) 501–505.
[20] H.F. Lopez, Identification of intermetallic phases in an automotive grade Aluminum A319 alloy, Mater. Perform. Charact. 6 (2017) 237–255.
[21] N. Chawla, R.S. Sidhu, V.V. Ganesh, Three-dimensional visualization and microstructure-based modeling of deformation in particle-reinforced composites, Acta Mater. 54 (6) (2006) 1541–1548.
[22] T. Hashimoto, G.E. Thompson, X. Zhou, et al., 3D imaging by serial block face scanning electron microscopy for materials science using ultramicrotomy, Ultramicroscopy 163 (2016) 6–18.
[23] L. Backerud, G. Chai, J. Tamminen, Solidification characteristics of aluminum alloys, Foundry Alloys 2 (1990) 71–84.
[24] D. Apelian, S. Shivkumar, G. Sigworth, Fundamental aspects of heat treatment of cast Al-Si-Mg alloys, Am. Foundry Soc. 97 (1989) 727–742.
[25] E. Sjölander, S. Seifeddine, The heat treatment of Al–Si–Cu–Mg casting alloys, J. Mater. Process. Technol. 210 (2010) 1249–1259.
[26] M. Zamani, S. Seifeddine, A.E.W. Jarfors, High temperature tensile deformation behavior and failure mechanisms of an Al–Si–Cu–Mg cast alloy — the microstructural scale effect, Mater. Des. 86 (2015) 361–370.
[27] C. Puncreobutr, P.D. Lee, K.M. Kareh, et al., Influence of Fe-rich intermetallics on solidification defects in Al–Si–Cu alloys, Acta Mater. 68 (15) (2014) 42–51.
[28] Q.G. Wang, C.H. Caceres, The fracture mode in Al–Si–Mg casting alloys, Mater. Sci. Eng., A 241 (1–2) (1998) 72–82.
[29] G.N. Grayson, G.B. Schaffer, J.R. Griffiths, Fatigue crack propagation in a sintered 2xxx series aluminium alloy, Mater. Sci. Eng., A 434 (1–2) (2006) 1–6.